

Quantum magnetotransport in a bilayer MoS₂: influence of a perpendicular electric field

M. Zubair¹, M. Tahir^{2,*}, P. Vasilopoulos³, and K. Sabeeh¹

¹*Department of Physics, Quaid-i-Azam University, Islamabad 45320, Pakistan*

²*Department of Physics, College of Science,
University of Hafr Al Batin, P.O. Box 1803,
Hafr Al Batin 31991, Kingdom of Saudi Arabia and*

³*Department of Physics, Concordia University,
Montreal, Quebec, Canada H3G 1M8*

Abstract

We first derive the energy dispersion of bilayer MoS₂ in the presence of a perpendicular electric field E_z . We show that the band gap and layer splitting can be controlled by the field E_z . Away from the k point, the intrinsic SOC splitting increases in the conduction band but is weakly affected in the valence band. We then analyze the band structure in the presence of a perpendicular magnetic field B and the field E_z , including spin and valley Zeeman terms, and evaluate the Hall and longitudinal conductivities. We discuss the numerical results as functions of the fields B and E_z for finite temperatures. The field B gives rise to a significant spin splitting in the conduction band, to a beating in the Shubnikov-de Haas (SdH) oscillations when it's weak, and to their splitting when it's strong. The Zeeman terms and E_z suppress the beating and change the positions of the beating nodes of the SdH oscillations at low B fields and enhance their splitting at high B fields. Similar beating patterns are observed in the spin and valley polarizations at low B fields. Interestingly, a 90% spin polarization and a 100% square-wave-shaped valley polarization are observed at high B fields. The Hall-plateau sequence depends on E_z . These findings may be pertinent to future spintronic and valleytronic devices.

I. INTRODUCTION

Recently the MoS₂ monolayer has provided a new testbed for the study of fermion physics in reduced dimensions. Its strong intrinsic SOC and huge band gap¹, approximately $2\lambda = 150$ meV and $2\Delta = 1.66$ eV, respectively, render it pertinent to potential applications in spintronics and optoelectronics²⁻⁵. Due to these features, MoS₂ may be more appropriate for device applications than graphene and the conventional two-dimensional electron gas (2DEG). Other investigated properties of monolayer MoS₂ are magnetocapacitance⁶, spin- and valley-dependent magneto-optical spectra⁷⁻⁹ and an unconventional quantum Hall effect (QHE)¹⁰. Most recently, magnetotransport studies of monolayer MoS₂ have been carried out¹¹⁻¹³.

In addition to monolayer MoS₂, it has been recently realized that bilayer MoS₂ has potential applications in optoelectronics and spintronics. Also, a band-gap tuning is possible in a MoS₂ bilayer in the presence of a perpendicular electric field E_z ¹⁴⁻¹⁶. Additional reported properties of bilayer MoS₂ include magnetoelectric effects and valley-controlled spin-quantum gates¹⁷, tuning of the valley magnetic moment¹⁸, and electrical control of the valley-Hall effect¹⁹. Moreover, a field-effect transistor has been realized experimentally in a few-layer MoS₂²⁰. In contrast, bilayer graphene has intrinsically a very weak SOC^{21,22} and, when not biased, a zero band gap²³⁻²⁵. There exist numerous theoretical and experimental^{24,26-29} studies of magnetotransport properties in bilayer graphene. Although its band gap can be controlled by an electric field E_z ³⁰⁻³³, high-quality samples of MoS₂ bilayers with a strong intrinsic SOC and a huge band gap are of particular importance. Contrary to bilayer graphene, the MoS₂ bilayer has greater potential for future spintronic and valleytronic applications. Recently, not only the QHE but also the SdH oscillations have been observed in high-quality monolayer and multilayer MoS₂³⁴ but neither magnetotransport nor the effect of an electric field E_z have, to our knowledge, been theoretically studied for bilayer MoS₂. Such a study is the aim of the present work.

The paper is organized as follows. In Sec. II we formulate the problem and discuss the band structure of bilayer MoS₂ with the help of the eigenvalues, eigenfunctions, Fermi energy, and density of states (DOS). We then evaluate the Hall and longitudinal conductivities using the linear-response formulas of Ref. 35. Interestingly, we find that the Hall-plateau sequence depends on the field E_z and becomes unconventional when E_z is present. Also, we compare

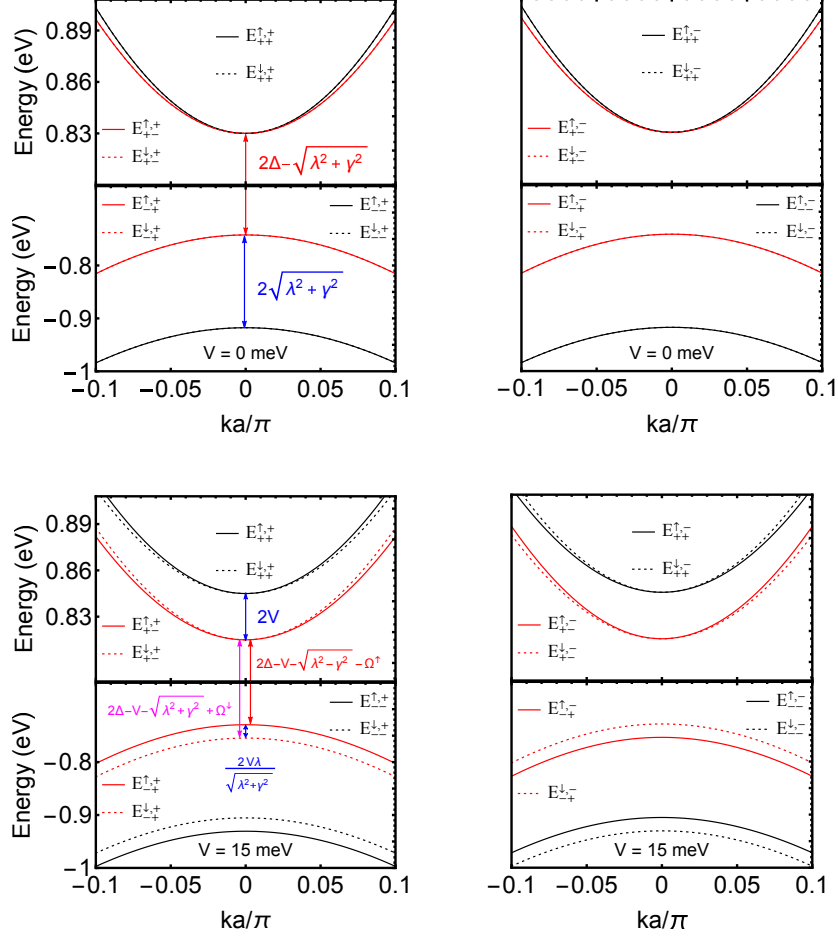


FIG. 1. Band structure of bilayer MoS₂ for $\lambda = 0.074$ eV and $\gamma = 0.047$ eV. The upper panels are for zero electric field energy ($V = 0$) and the lower ones for $V = 15$ meV. The left (right) panels are for the K (K') valley and $\Omega^s = s\lambda V/[\lambda^2 + \gamma^2]^{1/2}$.

the results with those on bilayer graphene. Concluding remarks follow in Sec. IV.

II. FORMULATION AND ELECTRONIC SPECTRUM

The one-electron Hamiltonian of bilayer MoS₂ near the K and K' valleys^{17,18,36,37} reads

$$H^\tau = \begin{pmatrix} -\xi_1^{s\tau} & v_F \pi_-^\tau & \gamma & 0 \\ v_F \pi_+^\tau & \xi_2^{s\tau} & 0 & 0 \\ \gamma & 0 & -\xi_3^{s\tau} & v_F \pi_+^\tau \\ 0 & 0 & v_F \pi_-^\tau & \xi_4^{s\tau} \end{pmatrix}. \quad (1)$$

Here, $\tau = 1(-1)$ is for K (K') valley, $\pi_\pm^\tau = \tau\pi_x \pm i\pi_y$, $\xi_1^{s\tau} = \kappa + \tau s\lambda + sM_z - \tau M_v$, $\xi_2^{s\tau} = \alpha - sM_z + \tau M_v$, $\xi_3^{s\tau} = \alpha - \tau s\lambda - sM_z + \tau M_v$, $\xi_4^{s\tau} = \kappa + sM_z - \tau M_v$ with $\kappa = \Delta + V$

and $\alpha = \Delta - V$ with Δ the monolayer band gap. Further, $v_F = 0.53 \times 10^6$ m/s¹⁰ is the Fermi velocity, V the external electric field energy, λ the strength of the intrinsic SOC with spins up (down) represented by $s = +1(\uparrow)(s = -1(\downarrow))$, and γ the effective interlayer interaction energy. Moreover, $M_z = g' \mu_B B / 2$ is the Zeeman exchange field induced by ferromagnetic order, g' the Landé g factor ($g' = g'_e + g'_s$), and μ_B the Bohr magneton³⁸; $g'_e = 2$ is the free electron g factor and $g'_s = 0.21$ the out-of-plane factor due to the strong SOC in MoS₂. The term, $M_v = g'_v \mu_B B / 2$ breaks the valley symmetry of the levels and $g'_v = 3.57$ ³⁸. The valley splitting has been measured in very recent experiments^{39–42} and is theoretically shown to be approximately 30 meV by first-principles calculations⁴³. The eigenvalues $E_\mu^{s,\tau}(k)$ of Eq. (1), when the magnetic field is absent, are

$$E_\mu^{s,\tau}(k) = \hbar v_F \varepsilon_\mu^{s,\tau}(k). \quad (2)$$

The subscript $\mu = (\mu_1, \mu_2)$ is used to denote the positive and negative energies of the upper layer, by $\mu_1 = \pm 1$, and of the lower layer by $\mu_2 = \pm 1$. The factor $\varepsilon_\mu^{s,\tau}(k) \equiv \varepsilon$ in Eq. (2) is the solution of the fourth-degree equation

$$[(\varepsilon - \alpha')(\varepsilon + \kappa' - \tau s \lambda') - k^2][(\varepsilon - \kappa')(\varepsilon + \alpha' + \tau s \lambda') - k^2] - \gamma'^2(\varepsilon - \alpha')(\varepsilon - \kappa') = 0, \quad (3)$$

where $k \equiv k_y$ is the wave vector, $\varepsilon = E/\hbar v_F$, $\lambda' = \lambda/\hbar v_F$, $\kappa' = \kappa/\hbar v_F$, $\gamma' = \gamma/\hbar v_F$, and $\alpha' = \alpha/\hbar v_F$. In the combined limit $\lambda' \rightarrow 0$, $\kappa' \rightarrow 0$, $\alpha' \rightarrow 0$, we obtain the energy dispersion for bilayer graphene⁴⁴.

In the upper panels of Fig. 1 we plot the energy dispersion of bilayer MoS₂ for field $E_z = 0$ ($V = 0$ meV) at both valleys. We remark the following: (i) The splitting due to the SOC is zero in the conduction and valence bands even in the presence of SOC^{14–18,36,37}. (ii) The splitting due to interlayer hopping is zero in the conduction band but finite in the valence band^{14–18,36,37}. Further, the splitting in the valence band is a combined effect of inter-layer coupling and SOC given by $2[\lambda^2 + \gamma^2]^{1/2}$ at $k = 0$. This relation indicates that the valence band is still split for $\lambda = 0$ ³⁶. (iii) The gap between conduction and valence band edges is given by $2\Delta - [\lambda^2 + \gamma^2]^{1/2}$ for $k = 0$ ³⁶. Notice that the effects of SOC and interlayer coupling are negligible in the conduction band, near $k = 0$, while at large values of k the SOC effect dominates.

For a finite field E_z ($V = 15$ meV) we plot the energy spectrum in the lower panels of Fig. 1. We remark the following: (i) The SOC splitting is modified by the field E_z . We

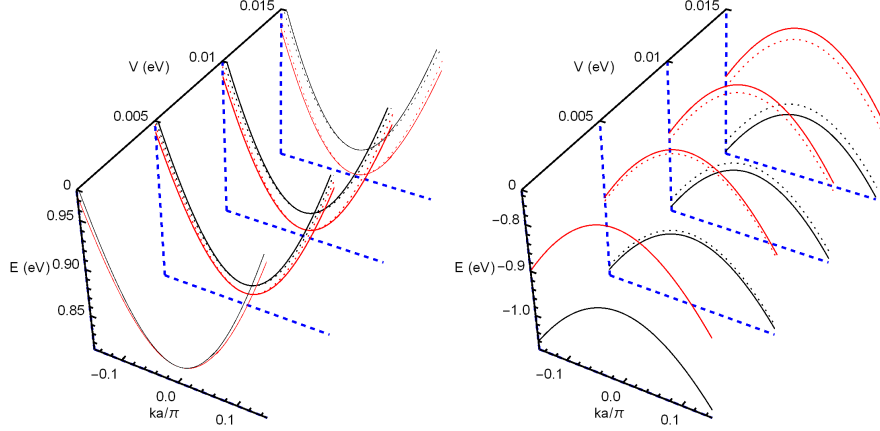


FIG. 2. Band structure of bilayer MoS₂ for different electric field E_z . The left (right) panel is for the conduction (valence) band. The curve marking and parameters are as Fig. 1.

also note that the spin splitting in the conduction band due to the SOC is negligible for the parameters and scale used. On the other hand, the valence band completely dictates the lifting of the spin degeneracy. (ii) An interlayer splitting is obtained in both the conduction and valence bands. Analytically we obtain the gaps $2V\lambda/[\lambda^2 + \gamma^2]^{1/2}$, for $V \ll \lambda$, and $2V$ at the valence and conduction band edges, respectively. (iii) The band gap is also reduced by the field $E_z \propto V$. It is equal to $2\Delta - V - [\lambda^2 + \gamma^2]^{1/2} - \tau_s\lambda V/[\lambda^2 + \gamma^2]^{1/2}$ for $V \ll \lambda$. The spin and layer splittings increase with the field E_z ^{15,16,48} or energy V , which can be seen in Fig. (2). So far we assumed that the band edges are at the K point of the Brillouin zone but this may not be the case neither for the valence band nor for the conduction band. In fact, there are arguments that our assumption holds^{3,17,18,45,46} but DFT calculations and a recent ARPES measurement⁴⁷ indicate that the valence band edge is shifted to the Γ point.

A. Landau levels

In the presence of a magnetic field B perpendicular to the layers we replace π by $-i\hbar\nabla + \mathbf{A}$ in Eq. (1) and take the vector potential \mathbf{A} in the Landau gauge $\mathbf{A} = (0, Bx, 0)$. After diagonalizing Eq. (1) the LL spectrum is obtained as

$$E_{n,\mu}^{s,\tau} = \hbar\omega_c \varepsilon_{n,\mu}^{s,\tau}, \quad (4)$$

where $\omega_c = v_F\sqrt{2eB/\hbar}$ is the cyclotron frequency. The subscript $\mu = (\mu_1, \mu_2)$ is used to denote the positive and negative energies in the upper ($\mu_1 = \pm 1$) and lower ($\mu_2 = \pm 1$)

layers. For $n \geq 1$ the factor $\varepsilon_{n,\mu}^{s,\tau} \equiv \varepsilon$ is the solution of the fourth-order equation

$$[(\varepsilon + d_1^{s\tau})(\varepsilon - d_2^{s\tau}) - n][(\varepsilon + d_3^{s\tau})(\varepsilon - d_4^{s\tau}) - (n+1)] - t^2(\varepsilon - d_2^{s\tau})(\varepsilon - d_4^{s\tau}) = 0, \quad (5)$$

where $t = \gamma/\hbar\omega_c$, $d_1^{s\tau} = \kappa^\tau + s\lambda + \tau(sM_z - \tau M_v)/\hbar\omega_c$, $d_2^{s\tau} = \alpha^\tau - \tau(sM_z - \tau M_v)/\hbar\omega_c$, $d_3^{s\tau} = \alpha^\tau - s\lambda - \tau(sM_z - \tau M_v)/\hbar\omega_c$, and $d_4^{s\tau} = \kappa^\tau + \tau(sM_z - \tau M_v)/\hbar\omega_c$ with $\kappa^\tau = \Delta + \tau V$ and $\alpha^\tau = \Delta - \tau V$ are dimensionless parameters. The eigenfunctions are

$$\psi_{n,\mu}^{s,+} = \frac{1}{\sqrt{L_y}} \begin{pmatrix} \varrho_{n,\mu}^{s,+} \phi_n \\ \Theta_{n,\mu}^{s,+} \phi_{n-1} \\ \Lambda_{n,\mu}^{s,+} \phi_n \\ \Upsilon_{n,\mu}^{s,+} \phi_{n+1} \end{pmatrix} e^{iky y}, \quad \psi_{n,\mu}^{s,-} = \frac{1}{\sqrt{L_y}} \begin{pmatrix} \Lambda_{n,\mu}^{s,-} \phi_n \\ \Upsilon_{n,\mu}^{s,-} \phi_{n+1} \\ \varrho_{n,\mu}^{s,-} \phi_n \\ \Theta_{n,\mu}^{s,-} \phi_{n-1} \end{pmatrix} e^{iky y}. \quad (6)$$

The coefficients are given by $\Theta_{n,\mu}^{s,\tau} = \sqrt{n} \varrho_{n,\mu}^{s,\tau}/[\varepsilon_{n,\mu}^{s,\tau} - d_2^{s\tau}]$, $\Lambda_{n,\mu}^{s,\tau} = k_{n,\mu}^{s,\tau} \varrho_{n,\mu}^{s,\tau}$, and $\Upsilon_{n,\mu}^{s,\tau} = \sqrt{n+1} k_{n,\mu}^{s,\tau} \varrho_{n,\mu}^{s,\tau}/[\varepsilon_{n,\mu}^{s,\tau} - d_4^{s\tau}]$, with $\varrho_{n,\mu}^{s,\tau}$ the normalization constants

$$\varrho_{n,\mu}^{s,\tau} = \left\{ (k_{n,\mu}^{s,\tau})^2 [1 + (n+1)/(\varepsilon_{n,\mu}^{s,\tau} - d_4^{s\tau})^2] + 1 + n/(\varepsilon_{n,\mu}^{s,\tau} - d_2^{s\tau})^2 \right\}^{-1/2} \quad (7)$$

and $k_{n,\mu}^{s,\tau} = [(\varepsilon_{n,\mu}^{s,\tau} + d_1^{s\tau})(\varepsilon_{n,\mu}^{s,\tau} - d_2^{s\tau}) - n]/t(\varepsilon_{n,\mu}^{s,\tau} - d_2^{s\tau})$. Therefore, the wave function of bilayer MoS₂ is a mixture of Landau wave functions with indices $n-1$, n , and $n+1$.

In Eq. (6) the index n can take the values: $n = -1, 0, 1, \dots$. If n or $n \pm 1$ is negative the function ϕ_n or $\phi_{n \pm 1}$ is identically zero, i.e., $\phi_{-2} \equiv 0$ and $\phi_{-1} \equiv 0$. For $n = -1$ Eq. (6) is just $\psi_{-1}^{s,+} = (0, 0, 0, \phi_0)$ and $\psi_{-1}^{s,-} = (0, \phi_0, 0, 0)$, i.e., $\varrho_{n,\mu}^{s,\pm}$, $\Theta_{n,\mu}^{s,\pm}$, and $\Lambda_{n,\mu}^{s,\pm}$ are equal to zero. There is only one energy level per valley corresponding to $n = -1$. For $n = 0$, Eq. (6) has zero coefficients $\Theta_{n,\mu}^{s,+}$ and $\Theta_{n,\mu}^{s,-}$, which results in three energy levels for each valley. For other values of n , i.e., for $n \geq 1$, there are four eigenvalues of the Hamiltonian (1), corresponding to four Landau levels in a bilayer for a given valley $\tau = \pm 1$.

In addition, there are two special LLs of bilayer MoS₂. For $n = -1$ and $n = 0$, Eq. (1) takes, respectively, the forms

$$H_{n=-1}^+ = \xi_4^+, \quad H_{n=-1}^- = \xi_2^- \quad (8)$$

and

$$H_{n=0}^+ = \begin{pmatrix} -\xi_1^{s+} & \gamma & 0 \\ \gamma & -\xi_3^{s+} & \hbar\omega_c \\ 0 & \hbar\omega_c & \xi_4^{s+} \end{pmatrix}, \quad H_{n=0}^- = \begin{pmatrix} -\xi_1^{s-} & \hbar\omega_c & \gamma \\ \hbar\omega_c & \xi_2^{s-} & 0 \\ \gamma & 0 & -\xi_3^{s-} \end{pmatrix}. \quad (9)$$

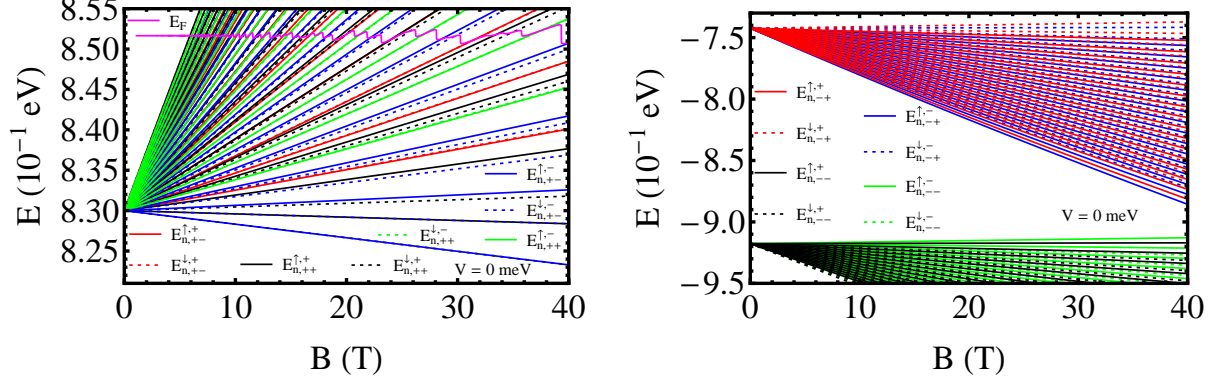


FIG. 3. Energy spectrum of bilayer MoS₂ versus magnetic field B for $M_z, M_v \neq 0$ and $V=0$. The left (right) panel is for the conduction (valence) band. The magenta curve shows the Fermi energy E_F versus B for an electron density $n_e = 1.9 \times 10^{13} \text{ cm}^{-2}$.

The factor ε corresponding to Eq. (9) is given by the roots of the cubic equation

$$(\varepsilon + d_1^{s\tau}) [(\varepsilon + d_3^{s\tau})(\varepsilon - d_4^{s\tau}) - 1] - t^2(\varepsilon - d_4^{s\tau}) = 0. \quad (10)$$

The corresponding eigenstates take the form

$$\psi_{0,\mu}^{s,+} = \frac{1}{\sqrt{L_y}} \begin{pmatrix} \varrho_{0,\mu}^{s,+} \phi_0 \\ 0 \\ \Lambda_{0,\mu}^{s,+} \phi_0 \\ \Upsilon_{0,\mu}^{s,+} \phi_1 \end{pmatrix} e^{ik_y y}, \quad \psi_{0,\mu}^{s,-} = \frac{1}{\sqrt{L_y}} \begin{pmatrix} \Lambda_{0,\mu}^{s,-} \phi_0 \\ \Upsilon_{0,\mu}^{s,-} \phi_1 \\ \varrho_{0,\mu}^{s,-} \phi_0 \\ 0 \end{pmatrix} e^{ik_y y}. \quad (11)$$

Note that Eqs. (10) give only three roots while μ provides four labels. We reserve the labels $\mu = (+, +)$ for the fourth root and denote by $\varepsilon_{-1,++}^{s,+} = d_4^{s,+}$ the corresponding eigenvalue for $n = -1$. We then write the respective LL state as $\psi_{-1,++}^{s,+} = (0, 0, 0, \phi_0)^T e^{ik_y y} / \sqrt{L_y}$, where T denotes the transpose of the row vector. Further, we reserve the label $\mu = (+, -)$ for $n = -1$ at the K' valley irrespective of the K valley, since the corresponding eigenvalue is $\varepsilon_{-1,+}^{s,-} = d_2^{s,-}$ and yields the state $\psi_{-1,+}^{s,-} = (0, \phi_0, 0, 0)^T e^{ik_y y} / \sqrt{L_y}$. The eigenfunctions depend on the quantum numbers n and k_y but the eigenvalues are independent of k_y .

B. Limiting cases

(i) Setting $\gamma = V = 0$ and $M_z = M_v = 0$ in Eq. (4) gives the eigenvalues of a MoS₂ monolayer or two uncoupled and unbiased layers

$$\varepsilon = -s\lambda_1 \pm [(\Delta' + s\lambda_1)^2 + (n+1)]^{1/2}, \quad \varepsilon = s\lambda_1 \pm [(\Delta' - s\lambda_1)^2 + n]^{1/2}, \quad (12)$$

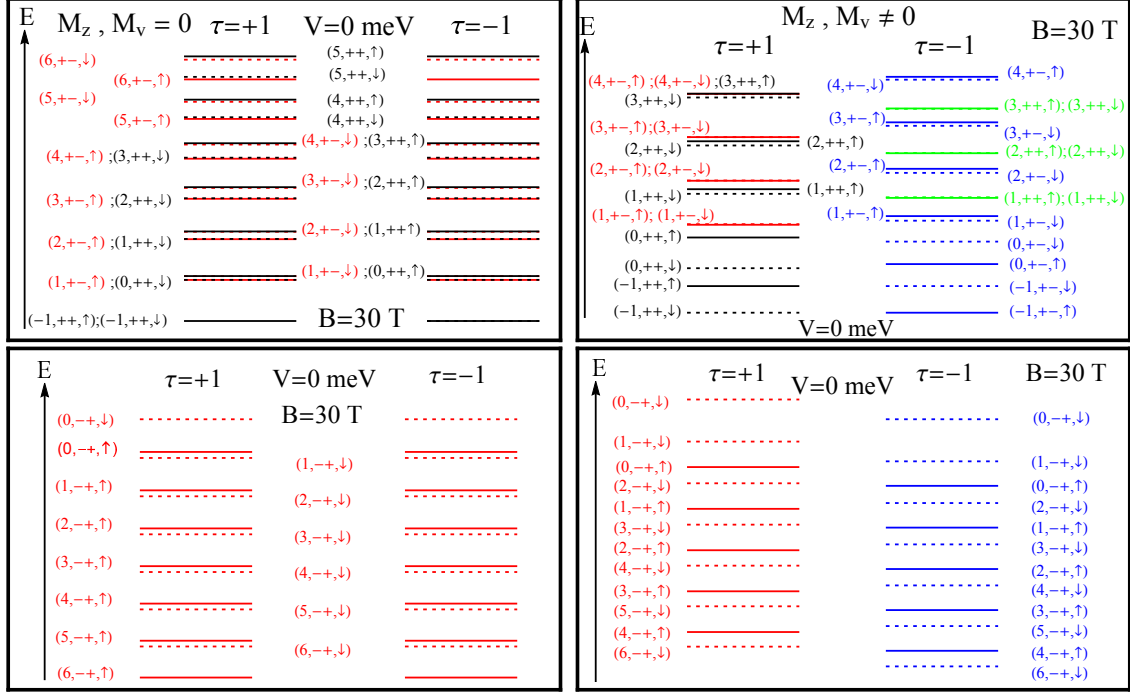


FIG. 4. LL spectrum of bilayer MoS₂ at $B = 30$ T and $V = 0$ labeled by (n, μ, s) with s the spin index $s = \pm 1(\uparrow\downarrow)$ and μ the layer index (see text after Eq. (4)) $\mu = (\mu_1\mu_2)$. The upper panels are for the conduction band and the lower ones are for the valence band. Further, the left panels are for $M_z = M_v = 0$ and the right ones for $M_z \neq M_v \neq 0$. For simplicity we do not show the valence band levels for the second layer.

where $\Delta' = \Delta/\hbar\omega_c$ and $\lambda_1 = \lambda/\hbar\omega_c$. These results are consistent with those in Refs. 11 and 12. If we set $\Delta' = \lambda_1 = 0$ in Eq. (12), we obtain the well-known eigenvalues for monolayer graphene⁴⁹

$$\varepsilon = \pm \sqrt{n+1}, \quad \varepsilon = \pm \sqrt{n}. \quad (13)$$

(ii) For $\Delta = \lambda = V = M_z = M_v = 0$, we obtain the LL spectrum of bilayer graphene²³⁻²⁵,

$$\varepsilon = \pm \frac{1}{\sqrt{2}} \left[t^2 + 2(2n+1) \pm [(t^2 + 2(2n+1))^2 - 16n(n+1)]^{1/2} \right]^{1/2}. \quad (14)$$

This equation can be further simplified by expanding the internal square root in the limit $n \ll t^2$. Moreover, by taking the negative sign, the solution is

$$\varepsilon = \pm 2\sqrt{n(n+1)}/t. \quad (15)$$

This spectrum is similar to that of Refs. 23 and 25 obtained by means of a 2×2 Hamiltonian.

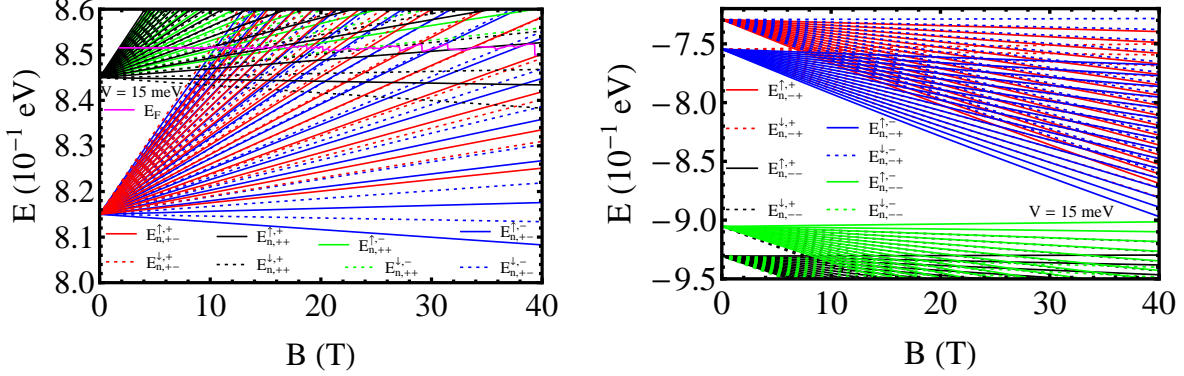


FIG. 5. As in Fig. 3 but for $V = 15$ meV.

The energy of higher LLs is obtained by taking the + sign in front of the internal square root in Eq. (14).

In Fig. 3 we plot the spectrum given by Eq. (4) versus the field B for $V = 0$ and finite spin M_z and M_v Zeeman fields. The left panel is for the conduction band and the right one for the valence band. The main findings are as follows. (i) The energy spectrum grows linearly with the field B due to the huge band gap. (ii) For $B = 0$ there are no LLs and the spin splitting in the conduction band, due to SOC, is very small^{14–18,36,37}, as seen in the upper panels of Fig. 1. But for a finite field B we obtain a significant spin splitting: for $B = 30$ T this is seen in the left panels of Fig. 4 and is due to the SOC alone, expressed by the term $\tau s \lambda$ in Eq. (1), since we intentionally set $M_z = M_v = 0$. The right panels in Fig. 4 are for $M_z \neq M_v \neq 0$. Interestingly, the spin splitting energy increases with B . Within the same LL $n = 10$ in the conduction band it is 1.4 meV at $B = 10$ T, 2.8 meV at $B = 20$ T, and 4.1 meV at $B = 30$ T. Further, one noteworthy feature is that the spin splitting among adjacent smaller-index LLs is unobservable, i.e. $E_{1,+}^{\uparrow(\downarrow),+} \cong E_{0,++}^{\downarrow(\uparrow),+}$ and $E_{0,+}^{\uparrow(\downarrow),-} \cong E_{1,++}^{\downarrow(\uparrow),-}$, whereas it is enhanced among the higher-index LLs due to the combined effect of the SOC and interlayer coupling terms in contrast with monolayer MoS₂¹². (iii) In the presence of the Zeeman fields the LL energies for spin up (down) at the K valley are different than those with spin down (up) at the K' valley and lead to spin and valley polarizations contrary to the $B = 0$ case in which they are the same^{14–18,36,37}. (iv) For $M_z \neq 0$ and $M_v = 0$ the spin splitting in the conduction band ($n = 10$) is 1.9 meV at $B = 10$ T, 3.7 meV at $B = 20$ T and 5.4 meV at $B = 30$ T. (v) The spin splitting among the lower and upper layer LLs at the K and K' valleys has vanished i.e. $E_{1,+}^{\uparrow,+} \cong E_{1,+}^{\downarrow,+}$ and $E_{2,+}^{\uparrow,-} \cong E_{2,+}^{\downarrow,-}$. This unexpected

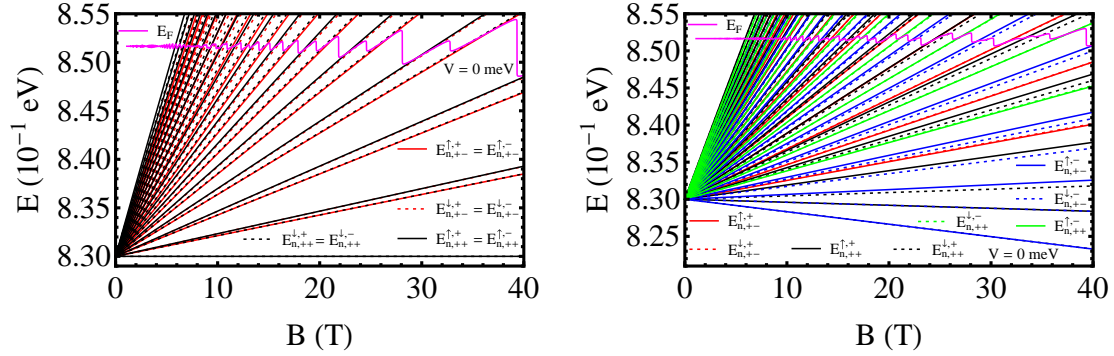


FIG. 6. LLs in bilayer MoS₂ (conduction band) vs the magnetic field B for $V = 0$ meV. The left panel is for $M_z = M_v = 0$, the right one for $M_z \neq M_v \neq 0$. The magenta curve shows E_F vs B .

behaviour of LLs is due to the presence of the $M_v \neq 0$ term. We also notice that the splitting is unobservable between other LLs e.g. $E_{4,+}^{\uparrow(\downarrow),+} \cong E_{3,++}^{\uparrow,+}$, $E_{8,+}^{\uparrow(\downarrow),+} \cong E_{9,+}^{\uparrow(\downarrow),-}$, $E_{9,+}^{\uparrow(\downarrow),+} \cong E_{8,++}^{\uparrow(\downarrow),-}$, $E_{14,+}^{\uparrow(\downarrow),+} \cong E_{13,++}^{\uparrow(\downarrow),+}$ and $E_{14,+}^{\uparrow(\downarrow),-} \cong E_{13,++}^{\uparrow(\downarrow),-}$. Such a behaviour of the LLs is absent in monolayer MoS₂¹². However, the value of the spin splitting is very strong in the valence band for both valleys. (vi) For $M_z = M_v = 0$, the $n = 0$ level is two-fold spin-split and valley degenerate in both the conduction and valence bands. For finite Zeeman fields though it is spin and valley non-degenerate in both the conduction and valence band. As for the $n = -1$ level, it is spin and valley degenerate for $M_z = M_v = 0$ whereas it is spin non-degenerate and valley degenerate for $M_z \neq M_v \neq 0$ in the conduction band ($\Delta \pm sM_z - M_v$) with plus (+) sign for the K valley and negative (-) sign for the K' valley; that is, the spin splitting is the same but opposite in both valleys. On the other hand, there is no level in the valence band for $n = -1$. These distinct features of the $n = 0$ and $n = -1$ levels can clearly be seen in Fig. 4. (vii) The LLs are unevenly spaced in the conduction band but equidistant in the valence band. This difference arises from the lack of electron-hole symmetry in our system. This unusual behavior of the LLs can clearly be seen in Fig. 4 for both zero and finite Zeeman fields.

We show the LL spectrum in Fig. 5 for finite field E_z ($V = 15$ meV) including the M_z and M_v terms. We deduce the following: (i) The field E_z modifies the inter-layer splitting, e.g., it makes it 30 meV in the conduction band. (ii) For $M_z = M_v = 0$ the LLs are still doubly degenerate consisting of a spin-up (\uparrow) state from the K valley and a spin-down (\downarrow) state from the K' valley. Furthermore, the $n = 0$ LL is spin non-degenerate but valley-degenerate in the conduction band. However, its spin and valley degeneracy are completely lifted in the

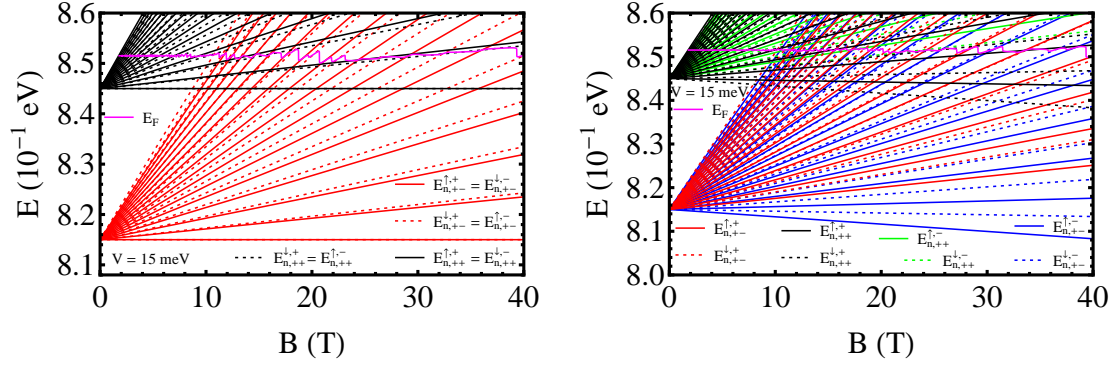


FIG. 7. As in Fig. 5 but for $V = 15$ meV.

valence band. Moreover, the valley degeneracy of the $n = -1$ level is lifted while its spin degeneracy in the conduction band is not. Interestingly, the spin splitting energy between adjacent LLs is also enhanced due to the finite field E_z . For example, for $n = 10$ its value is 1.9 meV at $B = 10$ T, 3.7 meV at $B = 20$ T, and 5.3 meV for $B = 30$ T. (iii) For $M_z \neq 0$ and $M_v = 0$ the spin splitting in the conduction band, for $n = 10$, is 3.2 meV at $B = 10$ T, 6.2 meV at $B = 20$ T, and 9.1 meV at $B = 30$ T. Additionally, the spin and valley degeneracies of all LLs in the conduction and valence bands are lifted. (iv) The energies of the LLs for the lower and upper layers have different slopes in B leading to level crossings. Interestingly, these crossings give rise to additional degeneracies of the levels. From Eq. (5) with $t = 0$, we obtain that these degeneracies, at specific energies and fields, are embodied in the relation

$$n_1 + n_2 = \varepsilon_{n_1}^2 + \varepsilon_{n_2}^2 + \varepsilon_{n_1}(d_1^{s\tau} - d_2^{s\tau}) + \varepsilon_{n_2}(d_3^{s\tau} - d_4^{s\tau}) - (d_1^{s\tau}d_2^{s\tau} + d_3^{s\tau}d_4^{s\tau}) - 1. \quad (16)$$

Here n_1 and n_2 indices label the LLs in the lower and upper layers, respectively. For $\Delta = \lambda = M_z = M_v = 0$ we obtain a relation similar to that in unbiased bilayer graphene²³. Also, though not shown, for $V \neq 0$ the LL spacing is not uniform in the conduction band whereas it is in the valence band and the spectra are similar to those in Fig. 4.

The Fermi energy E_F , at constant electron concentration n_e , is obtained from the relation

$$n_e = \int_{-\infty}^{\infty} D(E)f(E)dE = \frac{g_s/v}{D_0} \sum_{n,\tau,s,\mu} f(E_{n,\mu}^{s,\tau}), \quad (17)$$

where $f(E_{n,\mu}^{s,\tau}) = 1/[1 + \exp[\beta(E_{n,\mu}^{s,\tau} - E_F)]]$, $\beta = 1/k_B T$, is the Fermi-Dirac function, $D(E)$ the density of states (DOS), and $D_0 = 2\pi l_B^2$; $g_s(g_v)$ denotes the spin (valley) degeneracy.

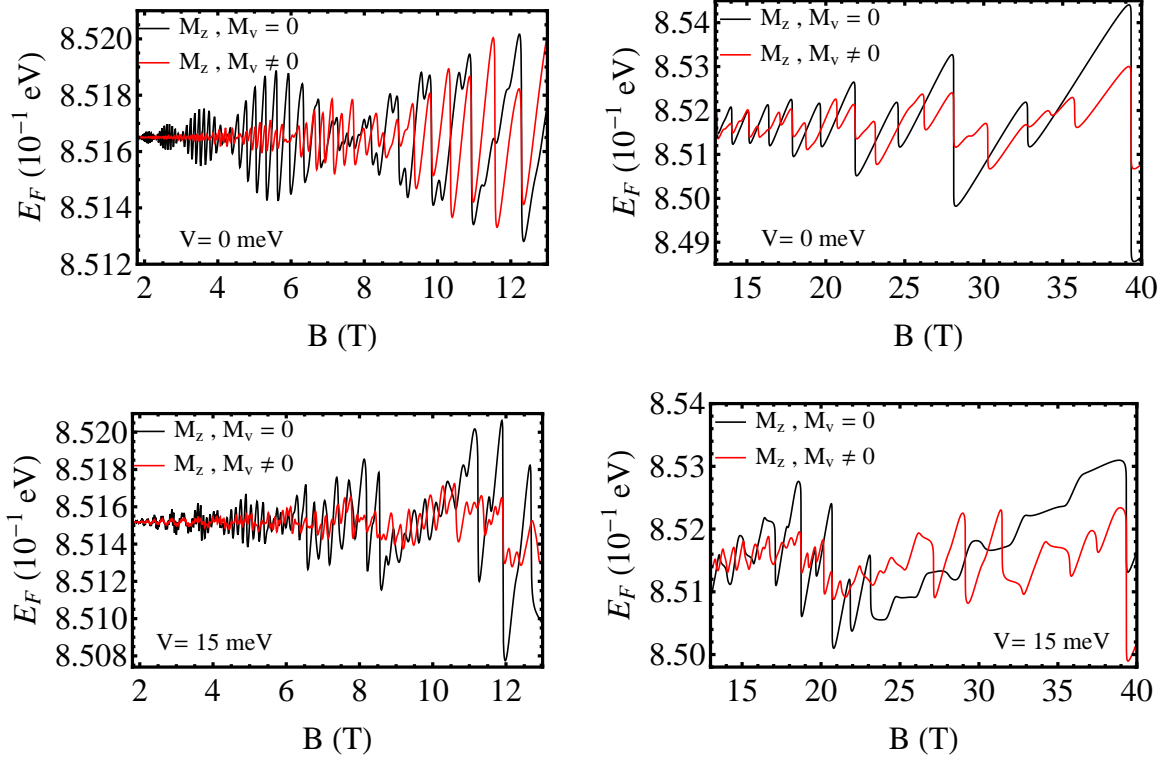


FIG. 8. Fermi energy E_F versus B at $T = 1$ K. The upper panels are for $V = 0$ meV and lower ones for $V = 15$ meV. The panels differ only in the range of B .

To better appreciate the difference between zero and finite Zeeman fields we redraw, in Fig. 6, the LL spectrum in the left panel for $M_z = M_v = 0$ and in the right one for $M_z \neq M_v \neq 0$ as functions of the magnetic field B . The LLs ($n \geq 0$) are spin non-degenerate and valley degenerate for $M_z = M_v = 0$ but for $M_z \neq M_v \neq 0$ the valley degeneracy is lifted. Nevertheless, the level for $n = -1$ is two-fold spin and valley-degenerate in the absence of the Zeeman terms but its spin degeneracy is lifted in their presence. The magenta solid lines in Fig. 6 show E_F versus the field B for $V = 0$ meV calculated numerically from Eq. (17). For zero Zeeman terms, the small intra-LL jumps indicate the presence of splitting due to SOC which is strengthened by the inter-layer coupling energy as seen in the left panel of Fig 6. However, the lifting of the spin and valley degeneracies due to finite Zeeman fields also give rise to additional intra LL small jumps in the E_F curve as can be seen in the right panel of Fig 6.

In Fig. 7 we replot the spectrum for $M_z = M_v = 0$ and $M_z \neq M_v \neq 0$ at $V = 15$ meV. We can see that the $n \geq 0$ levels are spin non-degenerate and valley degenerate for

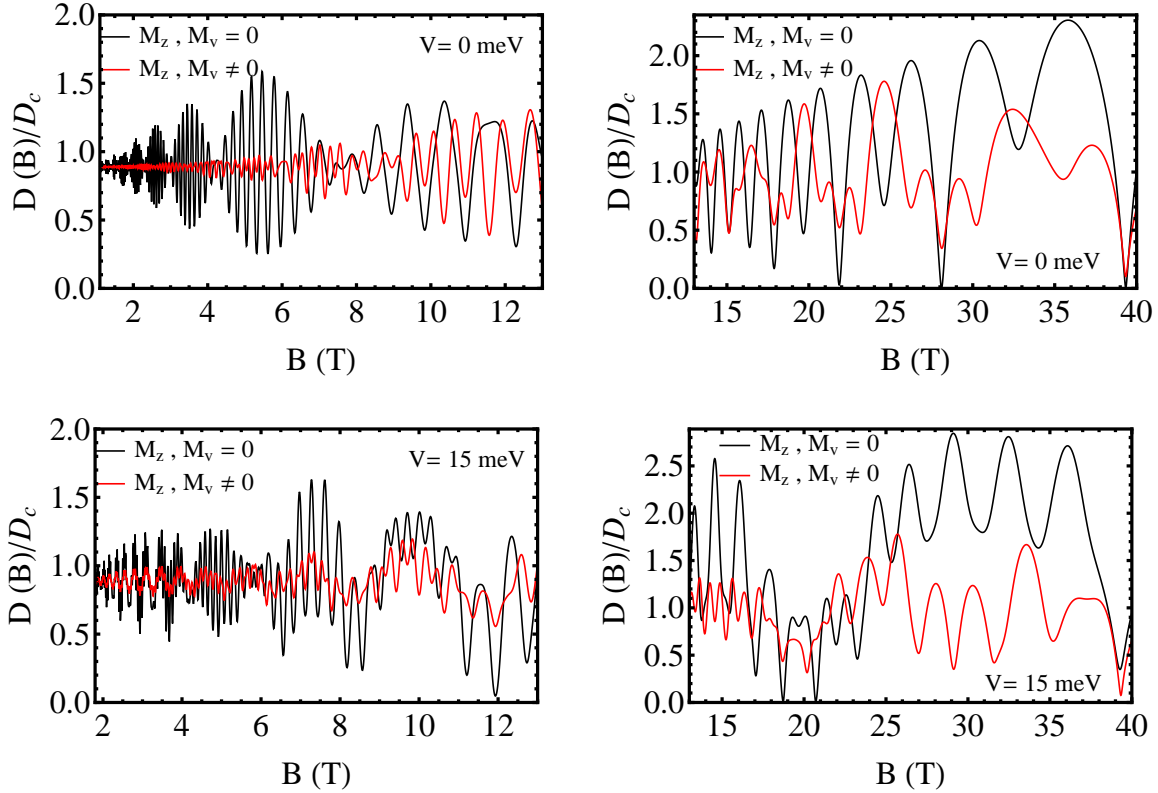


FIG. 9. Dimensionless density of states (DOS) with $D_c = g_{s/v}/D_0\Gamma\sqrt{2\pi}$ vs B for a LL width $\Gamma = 0.1\sqrt{B}$ meV. The upper panels are for $V = 0$ meV and the lower ones for $V = 15$ meV. The left and right panels differ only in the magnetic field range (x axis).

$M_z = M_v = 0$ whereas they are spin and valley non-degenerate for $M_z \neq M_v \neq 0$. On the other hand, the level for $n = -1$ is spin degenerate and valley non-degenerate in the absence of the Zeeman fields while its spin and valley degeneracies are lifted in their presence. For zero Zeeman fields (Fig. 7, left panel), the additional intra LL small jumps in the E_F curve are due to the spin and inter-layer splittings which are modified by the electric field E_z . However, the spin and valley non-degeneracies in the presence of the Zeeman fields lead to additional intra-LL small jumps in E_F as can be seen in the right panel of Fig. 7.

In Fig. 8 we show E_F as a function of the magnetic field for $V = 0$ meV and $V = 15$ meV. E_F shows not only the beating phenomenon at low fields $B \leq 13$ T but also dictates the giant splitting of the LLs at higher fields under the combined effect of spin and Zeeman terms as seen in the upper panels of Fig. 8. In the lower panels of Fig. 8 another worth noticing feature is the beating of the oscillations for B fields up to about 8 T with a giant splitting of the LLs at higher fields due the field E_z and the spin and valley Zeeman fields.

In Fig. 9 we plot the dimensionless DOS versus the field B in the conduction band for two different values of E_z . We observe a beating pattern at low fields B and a splitting at higher fields in the SdH oscillations. The former and latter characteristics are due to the splitting of the LLs by the combined effect of the SOC, interlayer coupling and Zeeman terms, and the layer splitting modified by the field E_z as seen by contrasting the curves of the upper and lower panels. One noteworthy feature is that the Zeeman fields and layer splitting suppress the amplitude of the beating at low B fields and enhance the oscillation amplitude at higher B fields. At higher B fields, the maximum SdH oscillation amplitude in the presence of the field E_z occurs due to the LL degeneracy which arises from the level crossings of the two layers. The inter-layer splitting and Zeeman effect change the position and number of the beating nodes as compared to monolayer MoS₂¹². We notice that in the conduction band the beating of the oscillations is observed in the range $0 \leq B \leq 13$ T, for $V = 0$ meV, and in the range $0 \leq B \leq 8$ T for $V = 15$ meV. Above these ranges the beating pattern is replaced by a split in the SdH oscillations. The particular beating oscillation pattern occurs when the level broadening is of the order of the cyclotron energy $\hbar\omega_c$ and is replaced by the split when the SOC becomes weak at larger fields B .

III. CONDUCTIVITIES

A. Hall conductivity

We use the linear-response theory as formulated in Ref. 35. If one uses the identity $f_\zeta(1 - f_{\zeta'})[1 - \exp(\beta(E_\zeta - E_{\zeta'}))] = (f_\zeta - f_{\zeta'})$, with f_ζ the Fermi-Dirac function, the Hall conductivity takes the simple form^{12,24,49,50},

$$\sigma_{yx} = \frac{i\hbar e^2}{L_x L_y} \sum_{\zeta \neq \zeta'} \frac{(f_\zeta - f_{\zeta'}) \langle \zeta | v_x | \zeta' \rangle \langle \zeta' | v_y | \zeta \rangle}{(E_\zeta - E_{\zeta'})^2}, \quad (18)$$

with $|\zeta\rangle = |n, \mu, s, \tau, k_y\rangle$ and $\langle \zeta | v_x | \zeta' \rangle$ and $\langle \zeta' | v_y | \zeta \rangle$ the off-diagonal matrix elements of the velocity operator. They are evaluated with the help of the corresponding operators $v_x = \partial H / \partial p_x$ and $v_y = \partial H / \partial p_y$, and are given in terms of the Pauli matrices σ_v

$$v_x = \tau v_F \begin{pmatrix} \sigma_x & 0 \\ 0 & \sigma_x \end{pmatrix}, v_y = v_F \begin{pmatrix} \sigma_y & 0 \\ 0 & -\sigma_y \end{pmatrix}, \quad (19)$$

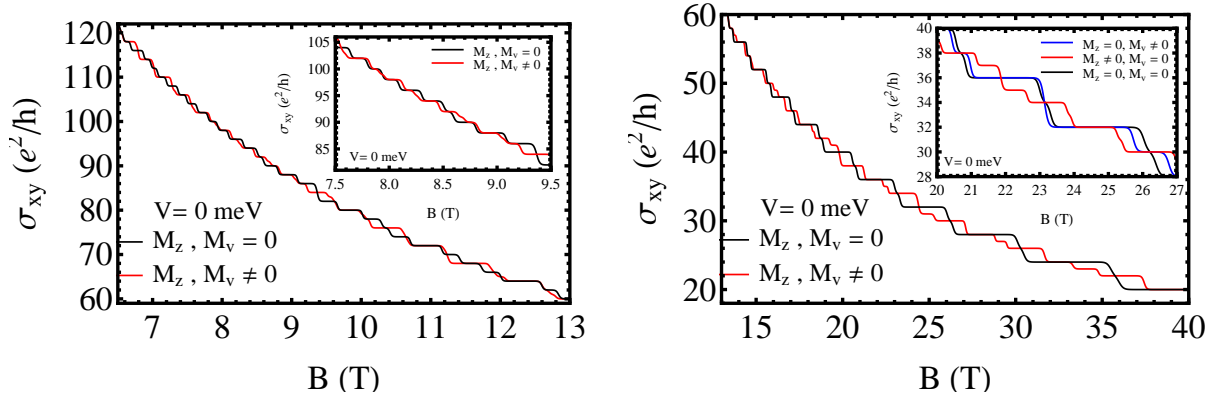


FIG. 10. Hall conductivity as a function of the magnetic field B for $T = 1$ K and $V = 0$ meV. The two panels differ only in the range of B . For further clarity, the range 7.5 T-9.5 T is shown in the inset to the left panel and the range 20 T-27 T in that to the right panel.

With $\varepsilon_{n,d_2} \equiv \varepsilon_{n,\mu}^{s,\tau} - d_2^{s\tau}$, $\varepsilon_{n,d_4} \equiv \varepsilon_{n,\mu}^{s,\tau} - d_4^{s\tau}$ and $Q = v_F \varrho_{n,\mu}^{s,\tau} \varrho_{n',\mu'}^{s',\tau'} \delta_{s,s'}$ the results are

$$\langle \zeta | v_x | \zeta' \rangle = \tau Q \left[\left(\frac{\sqrt{n'}}{\varepsilon'_{n,d_2}} + \frac{\sqrt{n+1} k_{n,\mu}^{s,\tau} k_{n',\mu'}^{s',\tau'}}{\varepsilon_{n,d_4}} \right) \delta_{n,n'-1} + \left(\frac{\sqrt{n}}{\varepsilon_{n,d_2}} + \frac{\sqrt{n'+1} k_{n,\mu}^{s,\tau} k_{n',\mu'}^{s',\tau'}}{\varepsilon'_{n,d_4}} \right) \delta_{n,n'+1} \right], \quad (20)$$

$$\langle \zeta' | v_y | \zeta \rangle = \tau i Q \left[\left(\frac{\sqrt{n'}}{\varepsilon'_{n,d_2}} + \frac{\sqrt{n+1} k_{n,\mu}^{s,\tau} k_{n',\mu'}^{s',\tau'}}{\varepsilon_{n,d_4}} \right) \delta_{n,n'-1} - \left(\frac{\sqrt{n}}{\varepsilon_{n,d_2}} + \frac{\sqrt{n'+1} k_{n,\mu}^{s,\tau} k_{n',\mu'}^{s',\tau'}}{\varepsilon'_{n,d_4}} \right) \delta_{n,n'+1} \right], \quad (21)$$

where $\mu = \{\mu_1, \mu_2\}$. Using Eqs. (18), (20), and (21) we obtain

$$\sigma_{yx} = \frac{e^2}{2h} \sum_{s,\tau,\mu,\mu'} \sum_n \left[\eta_{n,\mu,\mu'}^{s,\tau} \frac{f_{n,\mu}^{s,\tau} - f_{n+1,\mu'}^{s,\tau}}{(\varepsilon_{n,\mu}^{s,\tau} - \varepsilon_{n+1,\mu'}^{s,\tau})^2} - \varsigma_{n,\mu,\mu'}^{s,\tau} \frac{f_{n,\mu}^{s,\tau} - f_{n-1,\mu'}^{s,\tau}}{(\varepsilon_{n,\mu}^{s,\tau} - \varepsilon_{n-1,\mu'}^{s,\tau})^2} \right], \quad (22)$$

with

$$\eta_{n,\mu,\mu'}^{s,\tau} = (n+1) (\varrho_{n,\mu}^{s,\tau} \varrho_{n+1,\mu'}^{s,\tau})^2 \left[\frac{k_{n,\mu}^{s,\tau} k_{n+1,\mu'}^{s,\tau}}{\varepsilon_{n,d_4}} + \frac{1}{\varepsilon_{n+1,d_2}} \right]^2, \quad (23)$$

$$\varsigma_{n,\mu,\mu'}^{s,\tau} = n (\varrho_{n,\mu}^{s,\tau} \varrho_{n-1,\mu'}^{s,\tau})^2 \left[\frac{k_{n,\mu}^{s,\tau} k_{n-1,\mu'}^{s,\tau}}{\varepsilon_{n-1,d_4}} + \frac{1}{\varepsilon_{n,d_2}} \right]^2. \quad (24)$$

The second term in Eq. (22) is valid only for $n \geq 2$ while the first term is valid for $n \geq 1$. This is so because the sum over n is split in two parts, one for $n \geq 1$ and one for $n = 0$. Replacing $n-1$ with n in the second term and combining it with the first term, the sum

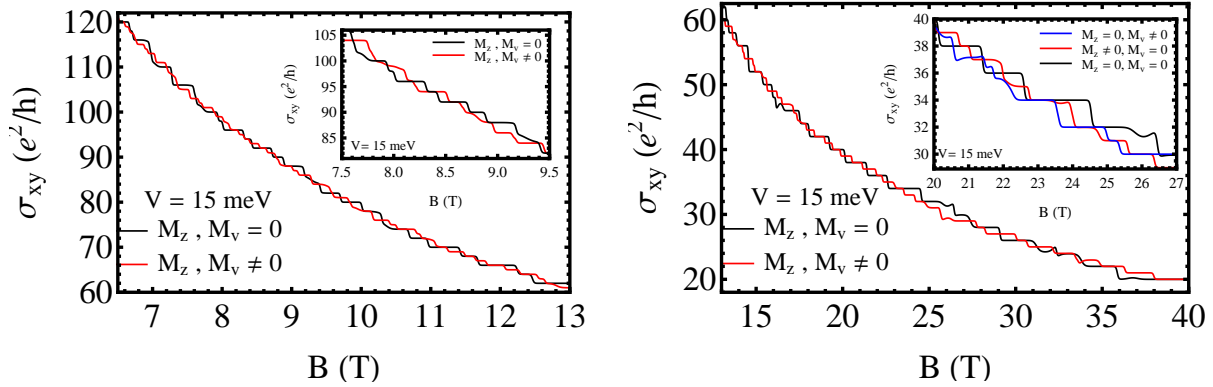


FIG. 11. Hall conductivity as a function of the magnetic field for $T = 1$ K and $V = 15$ meV. The two panels differ only in the range of B (x axis). For further clarity, the range 7.5 T - 9.5 T is shown in the inset to the left panel and the range 20 T - 27 T in that to the right one.

over n starts at $n = 1$ for both the terms. The $n = 0$ contribution to the Hall conductivity Eq. (22) is evaluated separately using the eigenstates (11). The result is given by Eq. (A5) in Appendix A. Furthermore, for the $n \geq 1$ LLs occupied, at $T = 0$, the $n = 0$ LL contribution to the Hall conductivity vanishes because all Fermi factors are equal to 1. In the limit $V = \Delta = \lambda = 0$, Eq. (22) reduces to similar ones for bilayer graphene^{24,25}.

Figure 10 shows the Hall conductivity as a function of the field B for $V = 0$ meV. We found that the height of the steps is not constant: there are two different heights: $2e^2/h$ and $4e^2/h$ see Fig. 10, black curve, in the absence of the spin and valley Zeeman terms. However, additional new heights $2e^2/h$, $3e^2/h$ and $4e^2/h$ emerge in the sequence ladder in their presence as the red curve shows. These differences result from vanishing spin splittings as discussed in detail below Eq. (15). Further, the plateaux in bilayer MoS₂ have different origin than those in bilayer graphene: the former are due to the strong SOC whereas the later result from strong interlayer coupling^{24,25}. A noteworthy feature of bilayer MoS₂ is that the influence of SOC and interlayer coupling is enhanced with increasing LL index and leads to new Hall plateaux as is evident from both panels of Fig. 10. In contrast to monolayer MoS₂¹², the plateaux in bilayer MoS₂ occur at higher magnetic fields.

We plot the Hall conductivity versus the field B in Fig. 11 for electric field energy $V = 15$ meV. For $M_z = M_v = 0$ (black curve of Fig. 11), the plateaux appear at 0, 2, 4,(e^2/h). It is noted that new plateaux like four step size multiples of e^2/h as seen in left and right panels of Fig. 11 (black curve) emerge at higher LLs due to level crossings caused by the

layer splitting. It is important to note that layer splitting is modified by a finite field E_z . On the other hand, additional plateaux emerge in the presence of spin and valley Zeeman fields, such as like $0, 1, 2, \dots(e^2/h)$. Interestingly, by contrasting Figs. 10 and 11 we see that the Hall plateau sequence strongly depends on the field E_z . Furthermore, when E_z is absent the plateaux occur at $0, 4, 8, 12, \dots(e^2/h)$ as depicted in Fig. 10 (black curve), whereas for a finite E_z , e. g., such that $V = 15$ meV, a new plateau sequence emerges with a mixture of double and quadruple steps of integral multiples of e^2/h , such as $0, 2, 4, 6, \dots(e^2/h)$ as shown in Fig. 11 (black curve). The latter is a result of layer splitting that is modified by the field E_z . The emergence of new steps in the Hall conductivity is directly connected to the small jumps in the Fermi level as shown by the purple curves in Figs. 6 and 7. Importantly, at higher B we find new plateaux in the Hall conductivity due to the spin and valley Zeeman fields in the absence and presence of the field E_z as the insets of Figs. 10 and 11 show.

B. Collisional conductivity

We assume that the electrons are elastically scattered by randomly distributed charged impurities. This type of scattering is dominant at low temperatures. If there is no spin degeneracy, the collisional conductivity is given by³⁵

$$\sigma_{xx} = \frac{\beta e^2}{L_x L_y} \sum_{\zeta, \zeta'} f(E_\zeta) [1 - f(E_{\zeta'})] W_{\zeta\zeta'} (x_\zeta - x_{\zeta'})^2. \quad (25)$$

Here $f(E_\zeta)$ is the Fermi-Dirac function, $\beta = 1/k_B T$, k_B is the Boltzmann constant, and E_F the chemical potential. $W_{\zeta\zeta'}$ is the transition rate between the one-electron states $|\zeta\rangle$ and $|\zeta'\rangle$ and e the electron's charge. Conduction occurs by hopping between spatially separated states centered at x_ζ and $x_{\zeta'}$, $x_\zeta = \langle \zeta | x | \zeta \rangle$. The rate $W_{\zeta\zeta'}$ in Eq. (25) is given by

$$W_{\zeta\zeta'} = \frac{2\pi N_I}{L_x L_y \hbar} \sum_q |U_q|^2 |G_{\zeta\zeta'}(r)|^2 \delta(E_\zeta - E_{\zeta'}) \delta_{k'_y, k_y + q}, \quad (26)$$

with $q^2 = q_x^2 + q_y^2$ and N_I the impurity density. For an impurity at the origin the screened potential is given by $U(\mathbf{r}) = e^2 e^{-k_s r} / \epsilon r$ and its Fourier transform $U_q = U_0 / [q^2 + k_s^2]^{1/2}$ with $U_0 = 2\pi e^2 / \epsilon$ and k_s the screening wave vector. Further, if the impurity potential is short ranged, of the Dirac δ -function type, one may use the approximation $k_s \gg q$ and obtain $U_q \approx U_0 / k_s$. $G_{\zeta\zeta'}(r) = \langle \zeta' | e^{i\mathbf{q}\cdot\mathbf{r}} | \zeta \rangle$ are the form factors and $|\zeta\rangle = |n, \mu, s, k_y\rangle$. Since the scattering by impurities is elastic and the spectrum is independent of k_y , we have $n = n'$

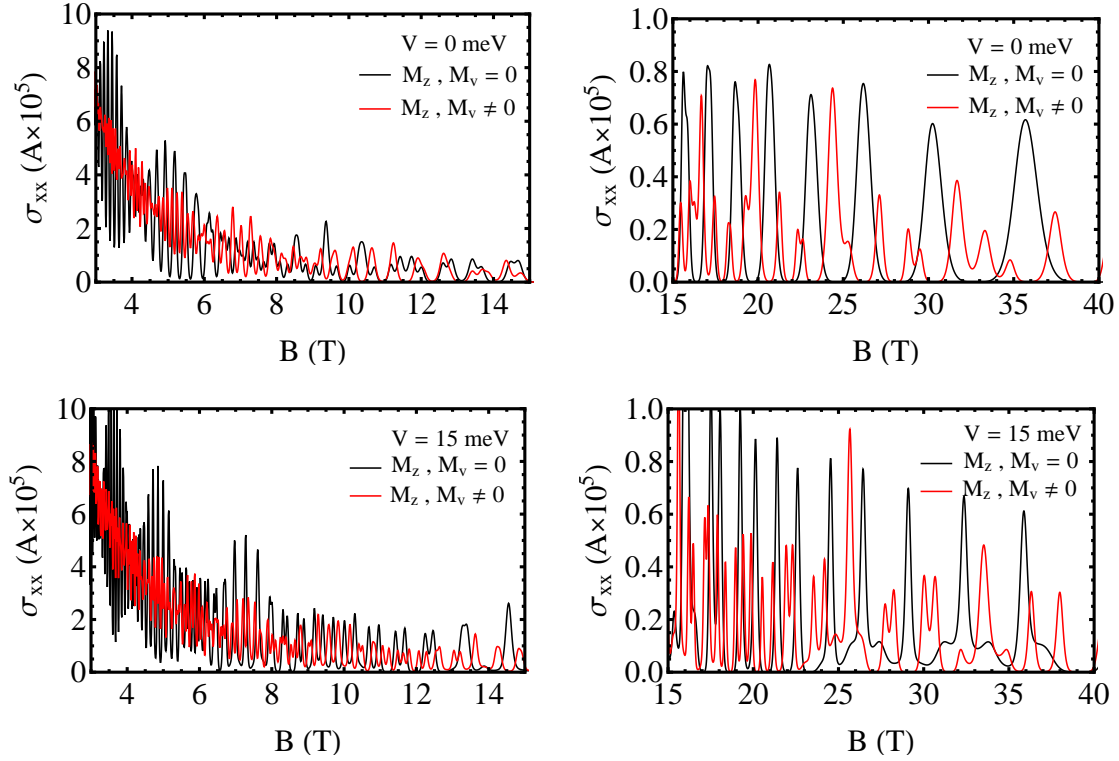


FIG. 12. Longitudinal conductivity versus magnetic field B at $T = 1$ K. The upper (lower) panels are for $V = 0$ meV ($V = 15$ meV). The left and right panels differ only in the range of B .

and no LL mixing. Further, $(x_\zeta - x_{\zeta'})^2 = l_B^4 q_y^2$. We notice that the eigenfunction oscillates around the centre of the orbit $x_0 = l_B^2 k_y$ and make the changes $\sum_{k_y} \rightarrow (L_y/2\pi) \int_{-k_0}^{k_0} dk_y$, $k_0 = L_x/2l_B^2$ and $\sum_q \rightarrow (L_x L_y/4\pi^2 l_B^2) \int_0^{2\pi} d\phi \int_0^\infty du$. The form factors $|G_{\zeta\zeta'}(u)|^2$ can be evaluated from the matrix element. For $n' = n, s = s', \mu = \mu'$ we obtain

$$|G_{nn}(u)|^2 = e^{-u} \left[[1 + (k_{n,\mu}^{s,\tau})^2] L_n(u) + \frac{n}{\varepsilon_{n,d_2}^2} L_{n-1}(u) + \frac{(n+1)(k_{n,\mu}^{s,\tau})^2}{\varepsilon_{n,d_4}^2} L_{n+1}(u) \right]^2, \quad (27)$$

with $u = l_B^2 q^2/2$ and $L_n(u)$ the associated Laguerre polynomials. Inserting all form factors in Eq. (25) and evaluating the integral over u in cylindrical coordinates gives

$$\sigma_{xx} = A \sum_{n,\mu,s,\tau} (\varrho_{n,\mu}^{s,\tau})^4 \left[(2n+1)[1 + (k_{n,\mu}^{s,\tau})^2]^2 + \frac{(2n-1)n^2}{\varepsilon_{n,d_2}^4} + \frac{(2n+3)(n+1)^2 (k_{n,\mu}^{s,\tau})^4}{\varepsilon_{n,d_4}^4} \right] \times f(E_{n,\mu}^{s,\tau}) [1 - f(E_{n,\mu}^{s,\tau})], \quad (28)$$

where $A = (e^2/h)(\beta N_I |U_0|^2 / \pi l_B^2 \Gamma k_s^2)$ and Γ is the level width. Note that Eq. (28) reduces to that for bilayer graphene²⁴ in the limit $V = \Delta = \lambda = 0$. The collisional conductivity for $n = -1, 0$ is given in Appendix B.

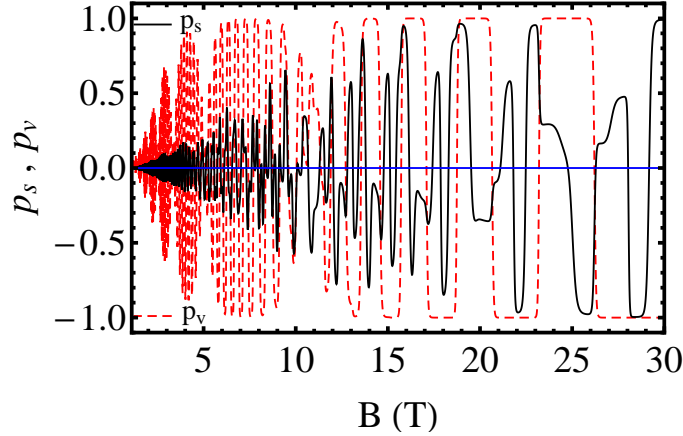


FIG. 13. Spin P_s and valley P_v polarizations versus magnetic field B at $T = 1$ K. The parameters are the same as in Fig. 11 for $M_z \neq M_v \neq 0$.

The longitudinal conductivity σ_{xx} , given by Eq. (28), is shown in Fig. 12 as a function of the field B for $E_z = 0$ (upper panels) and E_z finite (lower panels). In contrast to bilayer graphene, Fig. 12 shows a beating pattern of the SdH oscillations for B fields up to 9 T when E_z is absent ($V = 0$) and for B fields up to 7 T when a finite E_z is present ($V = 15$ meV). For high B fields the beating pattern is absent and the longitudinal conductivity peaks are split. The beating pattern is controlled by the fields E_z and B . A typical beating pattern occurs when the LL level broadening is of the same order as the LL separation. The SOC becomes weak at larger B fields. Interestingly, in contrast to monolayer MoS₂¹², the position of the nodes depends on both the field E_z and spin and valley Zeeman terms. The results of the collisional conductivity are consistent with the Fermi energy and DOS as seen in Figs. 8-9. Analytically, the beating of the SdH oscillations can be understood by making the approximation $\beta f(E_{n,\mu}^{s,\tau})[1 - f(E_{n,\mu}^{s,\tau})] \approx \delta(E_F - E_{n,\mu}^{s,\tau})$ at very low temperatures in Eq. (28), broadening the delta function, and carrying out the procedure followed in Ref. 12.

The spin P_s and valley P_v polarization, which are extracted from Eq. (28), are

$$P_s = \frac{(\sigma_{xx}^{K,\uparrow} + \sigma_{xx}^{K',\downarrow}) - (\sigma_{xx}^{K,\downarrow} + \sigma_{xx}^{K',\uparrow})}{(\sigma_{xx}^{K,\uparrow} + \sigma_{xx}^{K',\downarrow}) + (\sigma_{xx}^{K,\downarrow} + \sigma_{xx}^{K',\uparrow})}, \quad (29)$$

and

$$P_v = \frac{(\sigma_{xx}^{K,\uparrow} + \sigma_{xx}^{K,\downarrow}) - (\sigma_{xx}^{K',\uparrow} + \sigma_{xx}^{K',\downarrow})}{(\sigma_{xx}^{K,\uparrow} + \sigma_{xx}^{K,\downarrow}) + (\sigma_{xx}^{K',\uparrow} + \sigma_{xx}^{K',\downarrow})}. \quad (30)$$

We plot the spin P_s (black solid curve) and P_v (red dotted curve) polarization versus magnetic field at $T = 1$ K, $V = 0$ meV and finite Zeeman fields in Fig. 13. As expected

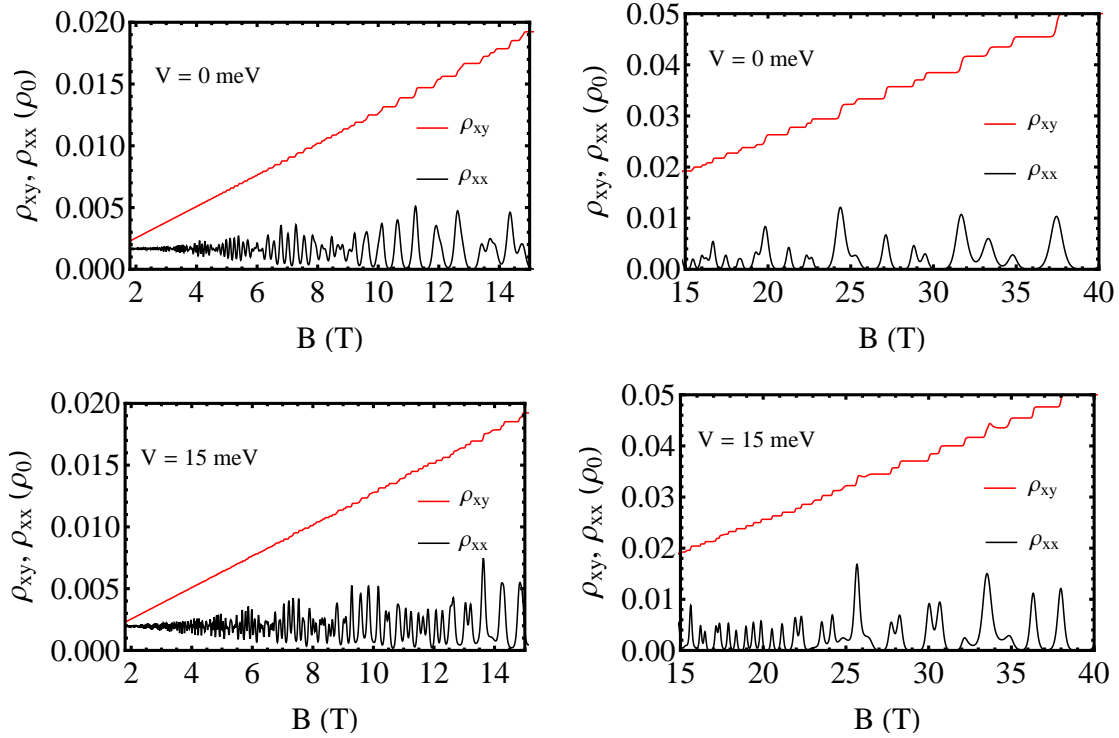


FIG. 14. Longitudinal (black) and Hall (red) resistivities versus magnetic field B at $T = 1$ K and finite spin and valley Zeeman fields. The upper panels are for $V = 0$ meV and the lower ones for $V = 15$ meV. The left and right panels differ only in the range of B and $\rho_0 = A^{-1} \times 10^{-35}$.

and can be seen, here too we have a beating pattern at low magnetic fields and well-resolved separation between both P_s and P_v at higher magnetic fields. The fact is that strong magnetic fields give rise to larger splittings of the LLs. In contrast to monolayer MoS_2 ¹², we find 100% valley polarization above $B > 13$ T whereas we attain 90% spin polarization above $B > 20$ T. Notice also the square-wave character of P_v above $B > 13$ T. However, for $M_z = M_v = 0$, there is no P_s and P_v as shown by the blue curve.

Finally, we evaluate the magnetoresistivity $\rho_{\mu\nu}$ using the conductivity tensor via the well-known relations $\rho_{xx} = \sigma_{xx}/S$ and $\rho_{xy} = \sigma_{xy}/S$ with $S = \sigma_{xx}\sigma_{yy} - \sigma_{xy}\sigma_{yx} \approx n_e^2 e^2 / B^2$ where n_e is the electron concentration. The Hall and longitudinal resistivities are shown in Fig. 14 versus magnetic field B for $T = 1$ K with field energy $V = 0$ meV (upper panels) $V = 15$ meV (lower panels). We observe extra plateaux in the Hall resistivity due to the SOC, layer splitting, and spin and valley Zeeman terms. The steps between the plateaux coincide with sharp peaks in the longitudinal resistivity. For $V = 0$ meV and strong B fields, larger than 13 T, we find a significant splitting of the Hall plateaux and the corresponding peaks

in the longitudinal resistivity due to spin and valley Zeeman fields. On the other hand, for $V = 15$ meV and B fields larger than 8 T, we find a well-resolved splitting of the Hall plateaux and the corresponding peaks of the longitudinal resistivity due to spin and valley Zeeman terms and inter-layer splitting. In contrast, for B fields less than 13 T ($V = 0$ meV) and 8 T ($V = 15$ meV), the longitudinal resistivities show a beating pattern. Importantly, this pattern is similar to that in a conventional 2DEG in the presence of the Rashba SOC⁵¹. Also, we note that well-resolved plateaux occur at relatively higher B than in monolayer MoS₂¹². We expect that these results will be verified by experiments.

IV. CONCLUSIONS

We studied quantum magnetotransport in bilayer MoS₂ in the presence of perpendicular electric (E_z) and magnetic (B) fields. At $B = 0$ we showed that there is no spin splitting for zero field E_z in both the conduction and valence bands whereas there is one for finite field E_z . Further, for $E_z \neq 0$ we demonstrated that the conduction band is still spin degenerate while the spin degeneracy in the valence band is fully lifted (see Fig. 1). We showed though that the layer splitting and band gap can be controlled by the field E_z . The spin degeneracy of the levels, for $E_z = 0$, in the conduction band, is lifted for $B \neq 0$ and is also enhanced linearly with B (see text after Eq. (15)). Furthermore, a finite field E_z leads to a significant enhancement of the spin splitting energy in the adjacent LLs of the conduction band. For $V = 0$ meV ($V = 15$ meV) and $B \leq 13$ T ($B \leq 8$ T), the Fermi energy E_F and DOS show a beating pattern which is replaced by a split of the SdH oscillations above $B > 13$ T ($B > 8$ T). Moreover, we showed that the combined action of spin and valley Zeeman fields and inter-layer splitting allow for intra-LL transitions and lead to new quantum Hall plateaux. The field E_z modifies the layer splitting. As a result, steps of various heights, in multiples of e^2/h (Fig. 11), occur in the Hall conductivity. Furthermore, for $V = 0$ meV ($V = 15$ meV) and $B > 9$ T ($B > 7$ T) the number of peaks in the longitudinal conductivity is doubled whereas for fields $B < 9$ T ($B < 7$ T) a beating pattern occurs similar to monolayer MoS₂¹² and the conventional 2DEG⁵¹.

Beating patterns, at low B fields, and splittings, at strong B fields, also occur in the spin and valley polarizations. It is worth emphasizing that a 100%, square-wave-shaped valley polarization is obtained for $B > 13$ T and 90% spin polarization for $B > 20$ T. The deep minima in the SdH oscillations are accompanied by Fermi level jumps and the peaks

coincide with the usual singularities of the DOS. A beating pattern and splitting of the SdH oscillations occur also in the resistivity that can be controlled by the magnetic field B which enhances the spin splitting in the conduction band. The spin and valley Zeeman fields lead to a giant splitting for strong B fields and to a lifting of the fourfold spin and valley degeneracies. The position of the plateaux as well as the peaks and beating pattern are sensitive to the field E_z and to the spin and valley Zeeman fields. The latter increase the number of beating nodes in the longitudinal conductivity, E_F , and DOS. The results, which we hope will be tested by experiments, indicate that bilayer MoS₂ is a promising alternative to bilayer graphene in the quest for gapped Dirac materials. We expect further applications of bilayer MoS₂ in the field of valleytronics and spintronics.

Acknowledgments: M. Z. and K. S. acknowledge the support of Higher Education Commission of Pakistan through project No. 20 – 1484/R&D/09 . K. S. also acknowledges the support of the Abdus Salam International Center for Theoretical Physics (ICTP) in Trieste, Italy, through the Associate Scheme where part of this work was completed. This work was supported by the the University of Hafr Al Batin (MT). The work of P. V. was supported by the Canadian NSERC Grant No. OGP0121756.

* (m.tahir06@alumni.imperial.ac.uk and tahir@uohb.edu.sa)

Appendix A: Zero-level Hall conductivity

Using Eqs. (11) the off-diagonal velocity matrix elements for $n = 0$ are

$$\begin{aligned} \langle 0, \mu, s, \tau | v_x | n', \mu', s', \tau' \rangle &= \tau v_F \varrho_{0,\mu}^{s,\tau} \varrho_{n',\mu'}^{s',\tau'} \delta_{s,s'} \\ &\times \left[\left\{ \frac{\sqrt{n'}}{\varepsilon'_{n,d_2}} + \frac{k_{0,\mu}^{s,\tau} k_{n',\mu'}^{s',\tau'}}{\varepsilon_{0,d_4}} \right\} \delta_{0,n'-1} + \frac{\sqrt{n'+1} k_{0,\mu}^{s,\tau} k_{n',\mu'}^{s',\tau'}}{\varepsilon'_{n,d_4}} \delta_{0,n'+1} \right], \quad (\text{A1}) \end{aligned}$$

$$\begin{aligned} \langle n', \mu', s', \tau' | v_y | 0, \mu, s, \tau \rangle &= \tau i v_F \varrho_{0,\mu}^{s,\tau} \varrho_{n',\mu'}^{s',\tau'} \delta_{s,s'} \\ &\times \left[\left\{ \frac{\sqrt{n'}}{\varepsilon'_{n,d_2}} + \frac{k_{0,\mu}^{s,\tau} k_{n',\mu'}^{s',\tau'}}{\varepsilon_{0,d_4}} \right\} \delta_{0,n'-1} - \frac{\sqrt{n'+1} k_{0,\mu}^{s,\tau} k_{n',\mu'}^{s',\tau'}}{\varepsilon'_{n,d_4}} \delta_{0,n'+1} \right]. \quad (\text{A2}) \end{aligned}$$

For $n = -1$ we find

$$\langle -1 | v_x | n', \mu', s', \tau' \rangle = \tau v_F \varrho_{n',\mu'}^{s',\tau'} k_{n',\mu'}^{s',\tau'} \delta_{s,s'} \delta_{0,n'}, \quad (\text{A3})$$

$$\langle n', \mu', s', \tau' | v_y | -1 \rangle = \tau i v_F \varrho_{n', \mu'}^{s', \tau'} k_{n', \mu'}^{s', \tau'} \delta_{s, s'} \delta_{0, n'}, \quad (\text{A4})$$

Using these expressions the Hall conductivity takes the form

$$\sigma_{yx} = \frac{e^2}{h} \sum_{s, \tau} \sum_{\mu, \mu'} \left[\eta_{0, 1, \mu, \mu'}^{s, \tau} \frac{f_{0, \mu}^{s, \tau} - f_{1, \mu'}^{s, \tau}}{(\varepsilon_{0, \mu}^{s, \tau} - \varepsilon_{1, \mu'}^{s, \tau})^2} + (\varrho_{0, \mu'}^{s, \tau} k_{0, \mu'}^{s, \tau})^2 \frac{f_{-1}^{s, \tau} - f_{0, \mu'}^{s, \tau}}{(\varepsilon_{-1}^{s, \tau} - \varepsilon_{0, \mu'}^{s, \tau})^2} \right], \quad (\text{A5})$$

where

$$\eta_{0, 1, \mu, \mu'}^{s, \tau} = (\varrho_{0, \mu}^{s, \tau} \varrho_{1, \mu'}^{s, \tau})^2 \left[\frac{1}{\varepsilon_{1, d_2}'} + \frac{k_{0, \mu}^{s, \tau} k_{1, \mu'}^{s, \tau}}{\varepsilon_{0, d_4}} \right]^2, \quad (\text{A6})$$

Appendix B: Zero-level collisional conductivity

The form factors for $n = 0$ and $n = -1$, with $n' = n$, $s = s'$, and $\mu = \mu'$, are given by

$$|G_{00}(u)|^2 = e^{-u} \left[[1 + (k_{0, \mu}^{s, \tau})^2] L_0(u) + \frac{(k_{0, \mu}^{s, \tau})^2}{\varepsilon_{0, d_4}^2} L_1(u) \right]^2, \quad (\text{B1})$$

and

$$|G_{-1-1}(u)|^2 = e^{-u} L_0^2(u) \quad (\text{B2})$$

The collisional conductivity is

$$\begin{aligned} \sigma_{xx} = A \sum_{\mu, s, \tau} \left[(\varrho_{0, \mu}^{s, \tau})^4 \left[[1 + (k_{0, \mu}^{s, \tau})^2]^2 + \frac{3(k_{0, \mu}^{s, \tau})^4}{\varepsilon_{0, d_4}^4} \right] f(E_{0, \mu}^{s, \tau}) [1 - f(E_{0, \mu}^{s, \tau})] \right. \\ \left. + f(E_{-1}^{s, \tau}) [1 - f(E_{-1}^{s, \tau})] \right], \quad (\text{B3}) \end{aligned}$$

-
- ¹ D. Xiao, G. Liu, W. Feng, X. Xu, and W. Yao, Phys. Rev. Lett. **108**, 196802 (2012).
² A. Ayari, E. Cobas, O. Ogundadegbe, and M. S. Fuhrer, J. Appl. Phys. **101**, 014507 (2007).
³ K. Mak, C. Lee, J. Hone, J. Shan, and T. Heinz, Phys. Rev. Lett. **105**, 136805 (2010).
⁴ B. Radisavljevic, A. Radenovic, J. Brivio, V. Giacometti, and A. Kis, Nat. Nanotech. **6**, 147 (2011).
⁵ A. Splendiani, L. Sun, Y. Zhang, T. Li, J. Kim, C.-Y. Chim, G. Galli, and F. Wang, Nano Lett. **10**, 1271 (2010).
⁶ X. Zhou, Y. Liu, M. Zhou, H. H. Shao, and G. H. Zhou, Appl. Phys. Express **7** 021201 (2014).

- ⁷ F. Rose, M. O. Goerbig, and F. Piechon, Phys. Rev. B **88**, 125438 (2013).
- ⁸ R.-L. Chu, X. Li, S. Wu, Q. Niu, W. Yao, X. Xu, and C. Zhang, Phys. Rev. B **90**, 045427 (2014).
- ⁹ Y.-H. Ho, Y.-H. Wang, and H.-Y. Chen, Phys. Rev. B **89**, 155316 (2014).
- ¹⁰ X. Li, F. Zhang, and Q. Niu, Phys. Rev. Lett. **110**, 066803 (2013).
- ¹¹ X. Zhou, Y. Liu, M. Zhou, D. Tang, and G. Zhou, J. Phys.: Condens. Matter **26**, 485008 (2014).
- ¹² M. Tahir, P. Vasilopoulos, and F. M. Peeters, Phys. Rev. B **93**, 035406 (2016).
- ¹³ A. Kormányos, P. Rakytá, and G. Burkard, New. J. Phys. **17**, 103006 (2015).
- ¹⁴ Q. Liu, L. Li, Y. Li, Z. Gao, Z. Chen, and J. Lu, J. Phys. Chem. C **116**, 21556 (2012).
- ¹⁵ A. Ramasubramaniam, D. Naveh, and E. Towe, Phys. Rev. B **84**, 205325 (2011).
- ¹⁶ N. Zibouche, P. Philipsen, A. Kuc, and T. Heine, Phys. Rev. B **90**, 125440 (2014).
- ¹⁷ Z. Gong, G.-B. Liu, H. Yu, D. Xiao, X. Cui, X. Xu, and Wang Yao, Nat. Commu. **4**, 15 (2013).
- ¹⁸ S. Wu, J. S. Ross, G. B. Liu, G. Aivazian, A. Jones, Z. Fei, W. Zhu, D. Xiao, W. Yao, D. Cobden, and X. Xu, Nat. Phys. **9**, 149 (2013).
- ¹⁹ J. Lee, K. F. Mak, and J. Shan, Nat. Nanotech. (2016).doi:10.1038/nnano.2015.337.
- ²⁰ A. T. Neal, H. Liu, J. J. Gu, and P. D. Ye, ACS Nano **7**, 7077 (2013).
- ²¹ F. Guinea, New J. Phys. **12**, 083063 (2010).
- ²² F. Mireles and J. Schliemann, New J. Phys. **14**, 093026 (2012).
- ²³ J. Milton Pereira, Jr., P. Vasilopoulos, and F. M. Peeters, Phys. Rev. B **76**, 115419 (2007).
- ²⁴ M. Zarenia, P. Vasilopoulos, and F. M. Peeters, Phys. Rev. B **85**, 245426 (2012).
- ²⁵ M. Nakamura, L. Hirasawa, and K. I. Imura, Phys. Rev. B **78**, 033403 (2008).
- ²⁶ K. Lee, S. Kim, M. S. Points, T. E. Beechem, T. Ohta, and E. Tutuc, Nano Lett. **11**, 3624 (2011).
- ²⁷ M. A. Hidalgo, and R. Cangas, arXiv:1602.02631.
- ²⁸ K. S. Novoselov, E. McCann, S. V. Morozov, V. I. Falko, M. I. Katsnelson, U. Zeitler, D. Jiang, F. Schedin, and A. K. Geim, Nat. Phys. **2**, 177 - 180 (2006).
- ²⁹ C. R. Dean, A. F. Young, I. Meric, C. Lee, L. Wang, S. Sorgenfrei, K. Watanabe, T. Taniguchi, P. Kim, K. L. Shepard, and J. Hone, Nat. Nanotech. **5**, 722 726 (2010).
- ³⁰ E. McCann, Phys. Rev. B **74**, 161403 (2006).
- ³¹ Y. Zhang, T.-T. Tang, C. Girit, Z. Hao, M. C. Martin, A. Zettl, M. F. Crommie, Y. R. Shen, and F. Wang, Nat. Phys. **459**, 820 (2009).

- ³² T. Ohta, A. Bostwick, T. Seyller, K. Horn, and E. Rotenberg, *Science* **313**, 951 (2006).
- ³³ F. Xia, D. B. Farmer, Y. Lin, and P. Avouris, *Nano Lett.* **10**, 715 (2010).
- ³⁴ X. Cui, G.-H. Lee, Y. D. Kim, G. Arefe, P. Y. Huang, C.-H. Lee, D. A. Chenet, X. Zhang, L. Wang, F. Ye, F. Pizzocchero, B. S. Jessen, K. Watanabe, T. Taniguchi, D. A. Muller, T. Low, P. Kim, and J. Hone, *Nat. Nanotechnol.* **10**, 534 (2015).
- ³⁵ M. Charbonneau, K. M. Van Vliet, and P. Vasilopoulos, *J. Math. Phys.* **23**, 318 (1982).
- ³⁶ A. M. Jones, H. Yu, J. S. Ross, P. Klement, N. J. Ghimire, J. Yan, D. G. Mandrus, W. Yao and X. Xu, *Nat. Phys.* **10**, 130 (2014).
- ³⁷ S. Fang, R. K. Defo, S. N. Shirodkar, S. Lieu, G. A. Tritsarlis, and E. Kaxiras, *Phys. Rev. B* **92**, 205108 (2015).
- ³⁸ A. Kormányos, V. Zólyomi, N. D. Drummond, and G. Burkard, *Phys. Rev. X* **4**, 011034 (2014).
- ³⁹ D. MacNeill, C. Heikes, K. F. Mak, Z. Anderson, A. Kormányos, V. Zólyomi, J. Park, and D. C. Ralph, *Phys. Rev. Lett.* **114**, 037401 (2015).
- ⁴⁰ A. Srivastava, M. Sidler, A. V. Allain, D. S. Lembke, A. Kis, and A. Imamoglu, *Nat. Phys.* **11**, 141 (2015).
- ⁴¹ G. Aivazian, Z. Gong, A. M. Jones, R.-L. Chu, J. Yan, D. G. Mandrus, C. Zhang, D. Cobden, W. Yao, and X. Xu, *Nat. Phys.* **11**, 148 (2015).
- ⁴² Y. Li, J. Ludwig, T. Low, A. Chernikov, X. Cui, G. Arefe, Y. D. Kim, A. M. van der Zande, A. Rigosi, H. M. Hill, S. H. Kim, J. Hone, Z. Li, D. Smirnov, and T. F. Heinz, *Phys. Rev. Lett.* **113**, 266804 (2014).
- ⁴³ Y. C. Cheng, Q. Y. Zhang, and U. Schwingenschlögl, *Phys. Rev. B* **89**, 155429 (2014).
- ⁴⁴ M. Koshino and T. Ando, *Phys. Rev. B* **81**, 195431 (2010).
- ⁴⁵ T. Cheiwchanamngij and W. R. L. Lambrecht, *Phys. Rev. B* **85**, 205302 (2012).
- ⁴⁶ A. Kumar and P. K. Ahluwalia, *Modelling Simul. Mater. Sci. Eng.* **21**, 065015 (2013).
- ⁴⁷ W. Jin, P.-C. Yeh, N. Zaki, D. Zhang, J. T. Sadowski, A. Al-Mahboob, A. M. v. d. Zande, D. A. Chenet, J. I. Dadap, I. P. Herman, P. Sutter, J. Hone, and R. M. Osgood, Jr. *Phys. Rev. Lett.* **111**, 106801 (2013).
- ⁴⁸ P. Koskinen, I. Fampiou, and A. Ramasubramaniam, *Phys. Rev. Lett.* **112**, 186802 (2014).
- ⁴⁹ P. M. Krstajic and P. Vasilopoulos, *Phys. Rev. B* **83**, 075427 (2011); *ibid.* **86**, 115432 (2012)
- ⁵⁰ M. Tahir, A. Manchon, and U. Schwingenschlögl, *Phys. Rev. B* **90**, 125438 (2014).
- ⁵¹ X. F. Wang and P. Vasilopoulos, *Phys. Rev. B* **72**, 085344 (2005); *ibid.* **67**, 085313 (2003).